



Fe₂O₃/P-doped CoMoO₄ electrocatalyst delivers efficient overall water splitting in alkaline media

Bowen Wang^{a,1}, Xiangxiong Chen^{a,b,1}, Yingjian He^{a,1}, Qin Liu^a, Xinxin Zhang^a, Ziyu Luo^a, John V. Kennedy^c, Junhua Li^d, Dong Qian^{a,*}, Jinlong Liu^{a,*}, Geoffrey I.N. Waterhouse^{e,*}

^a College of Chemistry and Chemical Engineering, Central South University, Changsha 410083, PR China

^b Yoening Tianci Mining Changsha Technology Center, Changsha 410083, PR China

^c National Isotope Centre, GNS Science, PO Box 30368, Lower Hutt 5010, New Zealand

^d College of Chemistry and Material Science, Hengyang Normal University, Hengyang 421008, PR China

^e School of Chemical Sciences, The University of Auckland, Auckland 1142, New Zealand

ARTICLE INFO

Keywords:

Electrochemical reconstruction

CoMoO₄-based catalyst

Phosphorization

Heterojunction

Overall water splitting

ABSTRACT

Phosphorization of molybdates has been shown to promote hydrogen evolution reaction (HER) activity but is usually detrimental to oxygen evolution reaction (OER) activity, frustrating efforts to create bifunctional HER/OER electrocatalysts. Herein, we show that Fe₂O₃-modulated P-doped CoMoO₄ on nickel foam (Fe-P-CMO) is an excellent bifunctional HER/OER electrocatalyst in alkaline media, with the adverse effect of phosphorization on the OER activity of CoMoO₄ being countered via Fe₂O₃ introduction. An alkaline splitting electrolyser assembled directly using the self-supporting Fe-P-CMO electrode possessed outstanding long-term durability with ultralow cell voltages of 1.48 and 1.59 V required to achieve current densities of 10 and 100 mA cm⁻², respectively. Detailed experimental investigations showed that during HER, P-doped CoMoO₄ in Fe-P-CMO underwent surface reconstruction with the *in-situ* formation of Co(OH)₂ on the P-CoMoO₄ (Co(OH)₂/P-CoMoO₄). During OER, P-doped CoMoO₄ was deeply reconstructed to CoOOH with the complete dissolution of Mo, leading to the *in-situ* formation of Fe₂O₃/CoOOH heterojunctions.

1. Introduction

Hydrogen is a very promising energy carrier owing to its high energy density (~282 kJ mol⁻¹), ability to be manufactured from various sources, and negligible CO₂ emissions when used as a fuel in hydrogen fuel cells [1–7]. Among various hydrogen production technologies, electrochemical water splitting utilizing the cathodic hydrogen evolution reaction (HER) and anodic oxygen evolution reaction (OER) is widely regarded as the simplest and most energy-efficient way of manufacturing hydrogen [8,9]. The kinetics of HER is fastest under acidic conditions. However, most of the oxides or (oxy)hydroxides commonly used as OER catalysts rapidly corrode in acidic media [10, 11]. Accordingly, alkaline water electrolysis is more practical and widely adopted in industry for scalable hydrogen production (even though the kinetics of HER is substantially slower in alkaline media due to the extra water-dissociation energy barrier in the Volmer step) [10, 12]. For alkaline water splitting, the rate of hydrogen production is

controlled by the kinetics of both OER and HER, motivating the search for high-performance electrocatalysts that can drive these reactions at high current densities and low overpotentials. Noble-metal-based Pt/C and IrO₂/RuO₂ catalysts represent the benchmark HER and OER catalysts, respectively, though the high cost and low earth abundance of the precious metals in these catalysts are obstacles to large-scale applications in industrial-scale water splitting [13–15]. Accordingly, researchers are now seeking electrocatalysts for HER or OER (including bifunctional HER/OER catalysts) based on first and second row transition metals, including metal carbides [16–18], oxides/hydroxides [19, 20], sulfides [21,22], nitrides [23], phosphides [24], and alloys [25]. Bifunctional HER/OER catalysts are especially desirable as a way of reducing process costs [26,27].

Among recently reported non-noble catalysts for HER, molybdate-based catalysts such as NiMoO₄ and CoMoO₄ are particularly promising [28,29]. Molybdates can easily be grown on the surface of nickel foam (NF) in the form of rods, flakes or other morphologies to create

* Corresponding authors.

E-mail addresses: qiangdong6@vip.sina.com (D. Qian), liujinlong@csu.edu.cn (J. Liu), g.waterhouse@auckland.ac.nz (G.I.N. Waterhouse).

¹ These authors contributed equally to this work.

self-supporting electrodes. [30–32] However, pure molybdates suffer from poor electrical conductivity and less than ideal H^+ adsorption ability on oxygen atoms for HER [33,34], motivating the search for strategies that can improve the catalytic performance of molybdate-based catalysts. Phosphorization is a simple strategy for boosting the catalytic performance of oxide-based catalysts for HER, with benefits including the modulation of the oxide's electronic structure, formation of abundant oxygen vacancies (OVs), and introduction of additional active sites [35–37]. It should be noted that oxygen sites and oxygen defective sites strongly influence the water dissociation step during HER. OVs not only improve the electronic conductivity but also change the interaction between the metal 3d and the O 2p bands of the catalyst, which is also important for OER [38,39]. In addition, identification of the true active sites in phosphorized molybdate-based catalysts is challenging [40–42]. During HER and OER, electrochemical reconstruction of molybdates [32,41–43] and transformation of phosphorous species [27,44,45] occur, making identification of active sites difficult. Owing to this uncertainty, various catalytic mechanisms have been reported for HER and OER on P-doped molybdate-based catalysts, including phosphide/molybdate interactions [40], hydroxide/P-doped molybdate interactions [42], and hydroxide/phosphide interactions [41]. Further, phosphorization of $NiMoO_4$ or $CoMoO_4$ (leading to P-doped molybdates) often produces catalysts with excellent HER activity but unchanged or even suppressed OER activity relative to the pristine molybdates [32,42,43]. Compared with the two-electron transfer reaction involved in the HER, the four-electron transfer OER is the “bottleneck” in overall water splitting. In this regard, it is crucial to produce molybdate-based catalysts with enhanced OER activity relative to their pristine counterparts to achieve efficient water electrolysis [46–48]. Heteroatom doping or constructing heterojunctions is an effective strategy for enhancing electrocatalyst activity and performance [48,49]. For example, the incorporation of Fe or Fe-based species into Ni/Co-oxide-based catalysts can improve OER and HER activities by forming a doping phase or regulating the electronic properties of active Ni and Co sites. [40,50–52]. To date, few studies have been reported for examining the effect of introduction of Fe or Fe-based species on the OER performance of $CoMoO_4$ -based catalysts. Accordingly, we hypothesized that the introduction of Fe or Fe-based species might boost the OER activity of $CoMoO_4$ -based catalysts while preserving (or even boosting) their excellent HER activity, thereby creating a novel bifunctional catalyst for overall water splitting under alkaline conditions. The technical challenge to verifying this hypothesis is how best to introduce Fe or Fe-based species to enhance both OER and HER performance. In addition to heteroatom doping effects, many studies have also established that during OER and HER creating heterojunctions can accelerate mass/charge transfer in different components, introduce more active sites at the heterointerfaces, tune energy barriers for the rate-determining steps, and improve reaction kinetics [53–55].

In this contribution, we prepared a novel Fe-P-CMO catalyst with an urchin-like structure. A $CoMoO_4$ /NF precursor was first prepared, with Fe then being incorporated in the precursor via ion exchange. Thermal phosphorization led to the P-doping of $CoMoO_4$, generation of abundant OVs, and the evolution of an Fe_2O_3 phase, with the resulting Fe_2O_3 /P- $CoMoO_4$ heterostructured catalyst on NF offering excellent bifunctional OER and HER activity in 1 M KOH. Subsequently, an efficient and robust alkaline electrolyser was constructed with Fe-P-CMO as both the cathode and anode catalysts. In addition, electrochemical reconstruction of the $CoMoO_4$ component was observed to occur during HER and OER, with the reconstruction processes studied in detail and the true active sites for HER and OER revealed.

2. Experimental section

2.1. Synthesis of CMO

Pieces of NF (1 cm × 5 cm) were ultrasonically cleaned in 3 M HCl

and then deionized (DI) water to remove surface oxides and other impurities. Next, 1.2 mmol of $Co(NO_3)_2 \cdot 6 H_2O$ and 0.3 mmol of $(NH_4)_6Mo_7O_{24} \cdot 2 H_2O$ were dissolved in 35 mL of DI water, and then the resulting solution was transferred to a 50 mL Teflon-lined autoclave. Subsequently, a piece of NF was placed vertically in the metal salt solution, and the autoclave was sealed and heated at 150 °C for 6 h to obtain purple $CoMoO_4$ on NF (CMO). The CMO was washed with DI water and then dried in air at 60 °C.

2.2. Syntheses of Fe-P-CMO and P-CMO

$K_3[Fe(CN)_6]$ (8 mg), trisodium citrate dihydrate ($C_6H_5Na_3O_7 \cdot 2 H_2O$, 25 mg), and polyvinylpyrrolidone (0.05 g) were dissolved in 20 mL of DI water to obtain an ion-exchange solution. CMO was then immersed in the ion-exchange solution for 9 h to form a CoFe Prussian blue analogue, i.e., $Co_3[Fe(CN)_6]_2$, on the surface. The obtained product is denoted hereafter as the $Co_3[Fe(CN)_6]_2$ /CMO precursor. After washing with DI water and drying, the $Co_3[Fe(CN)_6]_2$ /CMO precursor was transferred to an uncovered quartz boat in a tube furnace. Next, 1.2 g of $NaH_2PO_4 \cdot H_2O$ was placed in another uncovered quartz boat upstream of the quartz boat containing $Co_3[Fe(CN)_6]_2$ /CMO, with N_2 gas then flowed through the tube furnace. The furnace was heated to 400 °C at 5 °C min^{−1} and held at this temperature for 2 h to obtain a black Fe-P-CMO catalyst via phosphorization. In comparison, a P-CMO catalyst was synthesized by direct thermal phosphorization of CMO under the same conditions.

2.3. Synthesis of P-CFP

$Co_3[Fe(CN)_6]_2$ nanocubes were directly grown on the surface of NF according to a reported method [56], followed by thermal phosphorization at 400 °C for 2 h to obtain the P-CFP catalyst.

2.4. Syntheses of Pt/C and RuO_2 on NF

Catalyst inks were prepared by dispersing 20 wt% Pt/C (5.0 mg) or RuO_2 (5.0 mg) in a mixture containing 450 μL of ethanol, 500 μL of water, and 50 μL of a 5 wt% Nafion solution. The catalyst inks were then ultrasonically treated for 1 h to achieve homogeneous dispersions. Subsequently, 200 μL of catalyst ink was drop coated onto the surface of a freshly cleaned NF, and then the catalyst-modified foam allowed to dry in air at room temperature.

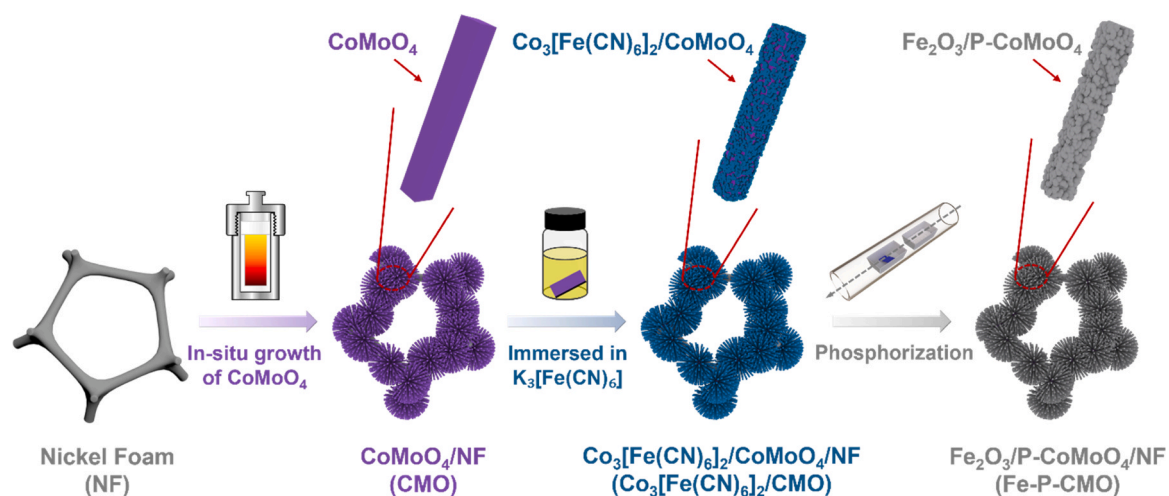
Chemicals, material characterizations, electrochemical measurements, and computation methods are specifically described in [Supporting Information](#).

3. Results and discussion

3.1. Catalyst structural characterization

Scheme 1 shows the preparation of Fe-P-CMO, involving hydrothermal, ion exchange, and thermal phosphorization steps. Hydrothermal treatment of NF in an aqueous solution containing $(NH_4)_2Mo_2O_7$ and $Co(NO_3)_2$ resulted in the growth of clusters of $CoMoO_4$ microrods on the surface of NF. The resulting precursor was then immersed in an etching solution containing $K_3[Fe(CN)_6]$ for 9 h to allow ion exchange between $K_3[Fe(CN)_6]$ and $CoMoO_4$. This led to the formation of cube-shaped $Co_3[Fe(CN)_6]_2$ particles of ~200 nm on $CoMoO_4$ microrods ($Co_3[Fe(CN)_6]_2$ /CMO) as shown in Fig. S1. Finally, thermal phosphorization at 400 °C yielded Fe-P-CMO, containing heterojunctions of Fe_2O_3 and P- $CoMoO_4$ microrods with abundant OVs on a NF support.

Scanning electron microscopy (SEM) was used to visualize the morphologies of products formed at each stage in the synthesis of Fe-P-CMO. The as-synthesized $CoMoO_4$ on NF (CMO) possessed an urchin-like structure composed of rods of tens-of-microns length (**Fig. 1a**). The microrods had smooth surfaces and diameters of 0.3 – 6 μm (inset of **Fig. 1a**). After partial etching in the $K_3[Fe(CN)_6]$ solution and



Scheme 1. Schematic showing the preparation of Fe-P-CMO.

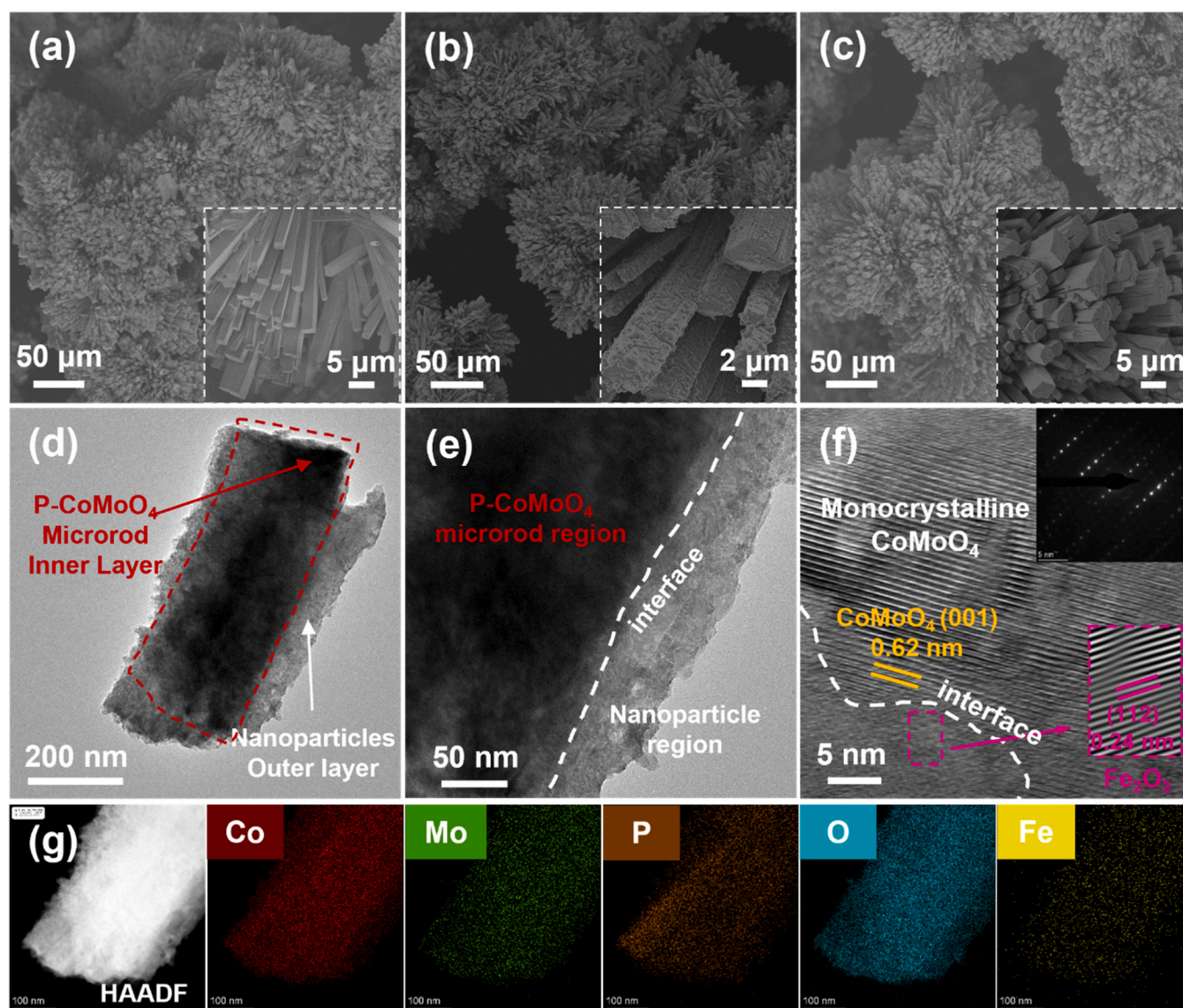


Fig. 1. SEM images of (a) CMO, (b) Fe-P-CMO, and (c) P-CMO; (d) TEM image of a representative stratified microrod in Fe-P-CMO; (e and f) HRTEM images of Fe-P-CMO (inset of f: SAED pattern of the CoMoO_4 microrod region in Fe-P-CMO); (g) Dark-field TEM image and corresponding EDS elemental maps of Fe-P-CMO.

phosphorization, the Fe-P-CMO catalyst retained a similar microrod structure, suggesting that the CoMoO_4 microrods had good structural stability (Fig. 1b). The enlarged SEM image (inset of Fig. 1b) showed a large number small nanoparticles on the surfaces of rods. In contrast, surfaces of the P-CMO catalyst (prepared directly from phosphorization of CMO without the ion exchange step) did not contain any nanoparticles (Fig. 1c) and still resembled CMO. The low-magnification transmission electron microscopy (TEM) image for Fe-P-CMO (Fig. 1d and e) confirmed a stratified rod-like structure, consisting of a P- CoMoO_4 microrod inner core surrounded by an outer layer of nanoparticles. The high-resolution TEM (HRTEM) image of Fe-P-CMO (Fig. 1f) showed lattice fringes with spacings of 0.24 and 0.62 nm, which could readily be assigned to the (112) planes of Fe_2O_3 and (001) planes of CoMoO_4 , respectively. The distinct boundary region between CoMoO_4 and Fe_2O_3 in Fig. 1f affirmed the successful formation of heterojunctions, which would enhance electron transfer and create new catalytically active sites at the heterointerfaces for HER and OER [53, 55]. The data suggested that Fe-P-CMO contained crystalline CoMoO_4 (P-doped, see below) coated with Fe_2O_3 nanoparticles. The presence of defects and regions of lattice disorder was observed for Fe-P-CMO (Fig. S2 for Fig. 1f), possible evidence for the presence of OV and unsaturated coordination of some metal atoms [57]. The large difference between the measured lattice fringe spacing of 0.62 nm and the theoretical value ($d=0.67$ nm) for the CoMoO_4 (001) planes offered further evidence for a large number of OV generated during the phosphorization step [37,39]. The selected area electron diffraction (SAED) pattern of a CoMoO_4 microrod in Fe-P-CMO confirmed that the rod possessed a single crystal nature (inset of Fig. 1f), which was expected to offer fast ion/electron transport during electrocatalysis [41]. Fig. 1g shows energy dispersive spectroscopy (EDS) results for Fe-P-CMO, revealing a very homogeneous distribution of Co, Mo, Fe, and O in the sample. P was less homogeneously distributed in the sample, the reason for which was discussed alongside the X-ray photoelectron spectroscopy (XPS) data for

Fe-P-CMO below.

The surface wettability of Fe-P-CMO was visualized by the water contact angle measurement (Fig. S3), demonstrating its superhydrophilicity. The superhydrophilic ability of Fe-P-CMO favored electrolyte adsorption and permeation, which was expected to maximize the active surface area and expedite the reaction kinetics during electrocatalytic water splitting [15,58].

Next, X-ray diffraction (XRD) was used to scrutinize the crystalline phases present in the as-prepared samples. The XRD pattern for the CMO precursor (Fig. S4) showed peaks due to $\text{CoMoO}_4 \cdot x\text{H}_2\text{O}$ (PDF#26-0477) and $\text{CoMoO}_4 \cdot 0.75\text{H}_2\text{O}$ [42], demonstrating two hydrated CoMoO_4 phases existing in the CMO precursor. In the XRD pattern of $\text{Co}_3[\text{Fe}(\text{CN})_6]_2/\text{CMO}$ (Fig. S4), except for peaks due to the CMO precursor, peaks corresponding to $\text{Co}_3[\text{Fe}(\text{CN})_6]_2 \cdot 10\text{H}_2\text{O}$ (PDF#46-0907) could be detected, affirming the formation of $\text{Co}_3[\text{Fe}(\text{CN})_6]_2$ on CMO when the CMO was immersed in an ion-exchange solution containing $\text{K}_3[\text{Fe}(\text{CN})_6]$. The XRD pattern of P-CMO (Fig. 2a) showed peaks due to NF and CoMoO_4 (PDF#21-0868), indicating that the thermal phosphorization step caused the dehydration of $\text{CoMoO}_4 \cdot x\text{H}_2\text{O}$. Fe-P-CMO showed XRD peaks due to NF, CoMoO_4 , and Fe_2O_3 (PDF#47-1409). The Fe_2O_3 (112) peak was very intense, suggesting preferential orientation (as shown in HRTEM, where lattice fringes due to Fe_2O_3 (112) facets were seen). No obvious XRD peaks due to metal phosphide or phosphate species were seen in the XRD patterns of P-CMO and Fe-P-CMO (if present, these phases must have been amorphous).

3.2. XPS analysis and reconstruction of Fe-P-CMO during HER and OER

XPS was applied to examine near surface region chemical compositions of Fe-P-CMO and P-CMO. The Co 2p spectrum of as-prepared Fe-P-CMO (Fig. 2b) showed two peaks at 782.1 and 797.9 eV in a 2:1 area ratio, which could readily be assigned to the Co $2p_{3/2}$ and Co $2p_{1/2}$ signals of Co^{2+} species, respectively [42]. A further set of peaks at 786.6

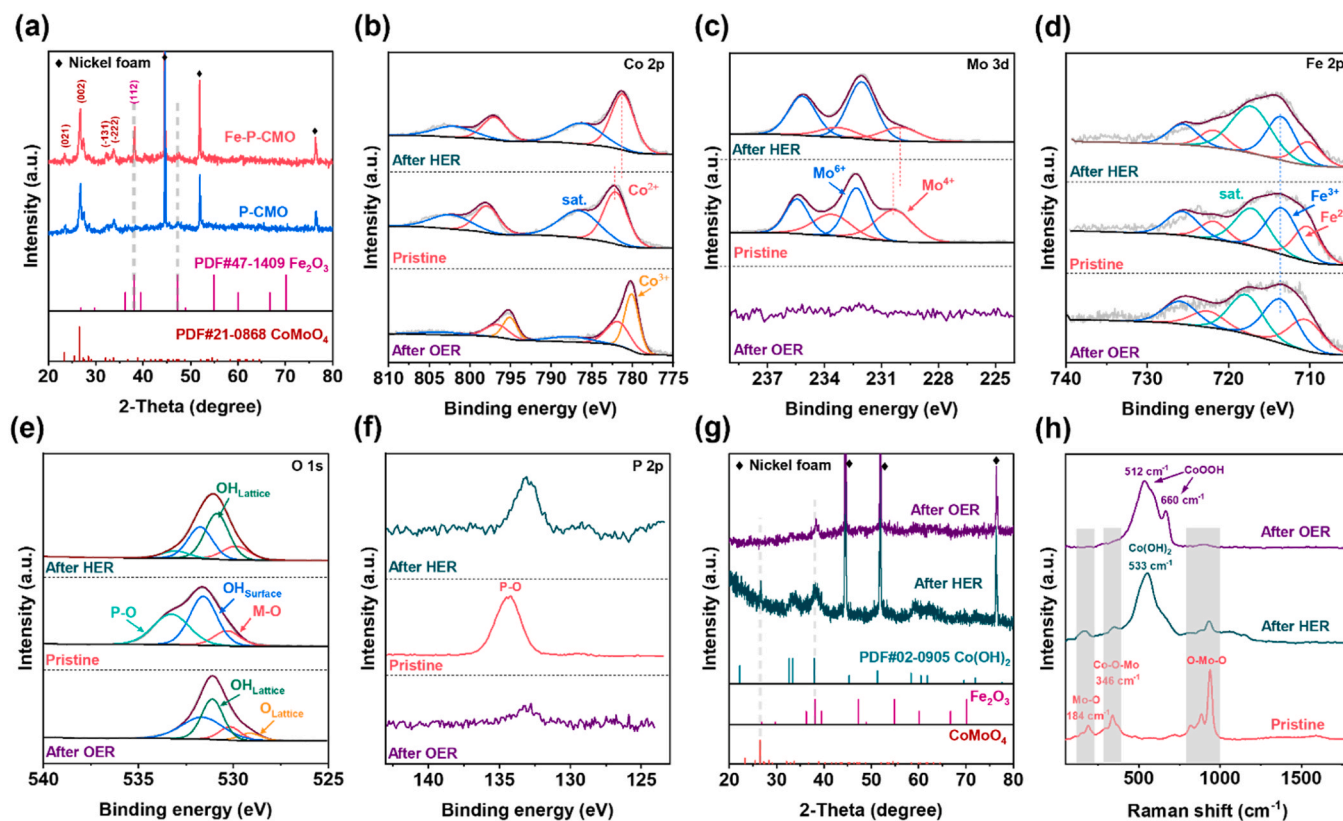


Fig. 2. (a) XRD patterns of Fe-P-CMO and P-CMO; high-resolution XPS spectra of (b) Co 2p, (c) Mo 3d, (d) Fe 2p, (e) O 1s, and (f) P 2p for Fe-P-CMO before and after OER and HER; (g) XRD patterns and (h) Raman spectra of Fe-P-CMO before and after OER and HER.

and 802.4 eV were due to Co^{2+} shake-up satellites. Compared with CMO, the Co 2p signals for P-CMO and Fe-P-CMO shifted to higher binding energy (Fig S4a), implying that the electron density of Co cations decreased upon the introduction of phosphorus [59,60]. The Mo 3d spectrum of as-prepared Fe-P-CMO (Fig. 2c) showed two sets of peaks, with each set having a fixed 3:2 area ratio. Peaks at 230.4 and 233.6 eV could readily be assigned to the Mo $3d_{5/2}$ and Mo $3d_{3/2}$ signals of Mo^{4+} species, whilst the second set of peaks at 232.3 and 235.5 eV were due to Mo^{6+} [40]. The Mo 3d spectrum of P-CMO was similar to that of Fe-P-CMO containing peaks for both Mo^{4+} and Mo^{6+} species, whereas the Mo 3d spectrum for CMO contained contributions from Mo^{6+} only (Fig S4b). We associate the low-valence Mo^{4+} species in Fe-P-CMO and P-CMO with OV's generated by surface oxide reduction in the PH_3 atmosphere released by heating $\text{NaH}_2\text{PO}_4 \cdot \text{H}_2\text{O}$ in N_2 [40,42]. Notably, negative shifts in binding energy from P-CMO to Fe-P-CMO could be found in both the Co 2p and Mo 3d spectra (Fig S4b), suggesting that more electrons accumulate around the P-doped CoMoO_4 after coupling with Fe_2O_3 to form heterogeneous interfaces [40]. The Fe 2p spectrum of Fe-P-CMO (Fig. 2d) showed peaks in the Fe $2p_{3/2}$ region at 710.4, 713.6 and 717.4 eV, which could readily be assigned to Fe^{2+} , Fe^{3+} , and a shake-up satellite signals, respectively [61]. The O 1s spectrum of Fe-P-CMO (Fig. 2f) was deconvoluted into three peaks, which were located at 530.2 eV (metal-O), 531.6 eV (surface OH), and 533.1 eV (P-O) [40,42]. The P 2p spectrum of Fe-P-CMO (Fig. 2f) contained a peak at 134.3 eV, typical for P-O species (e.g., PO_4^{3-}), which was bonded with Co^{2+} to yield Co-PO_4 species [42]. It has also been established that MoO_4^{2-} groups in CoMoO_4 are partially replaced by PO_4^{3-} groups during phosphorization, and the Co-PO_4 species are primarily generated on the surface of CoMoO_4 [42]. This would account for the less uniform distribution of the P element in the EDS spectrum (Fig. 1g).

Following HER in 1 M KOH, a number of changes were seen in the XPS spectra for Fe-P-CMO (Fig. 3). The Co 2p (Fig. 2b) and Mo 3d (Fig. 2c) XPS spectra shifted to lower binding energies after HER, implying the formation of new phases during HER. Further, the amount of Mo^{4+} in the near surface region of the sample decreased (Fig. 2c), suggesting surface leaching of Mo^{4+} . The Fe 2p spectrum was largely unaffected by HER (Fig. 2d), proving Fe_2O_3 being very stable under the polarization conditions of alkaline HER in 1 M KOH. In the O 1s (Fig. 2e) and P 2p spectra (Fig. 2f), peaks associated with the P-O species were significantly attenuated, suggesting leaching of the phosphate species during HER. Furthermore, the peaks associated with the P-O species shifted to the lower binding-energy region after both HER and OER, which were also observed in previous reports for related catalysts such as P-doped $\beta\text{-CoMoO}_4$ after HER and OER [42] and $\text{FeNiP}/\text{MoO}_x/\text{NiMoO}_4$ after an HER stability test [40]. This was probably due to the fact that MoO_4^{2-} groups in CoMoO_4 were partially replaced by PO_4^{3-}

groups to yield Co-PO_4 species during phosphorization, and the Co-PO_4 species were mostly generated on the surface of CoMoO_4 with a small part in the crystal lattice of the catalyst [42]. During both HER and OER, the leaching of PO_4^{3-} species occurred. Thus, negative shifts in binding-energy for peaks associated with P-O species could be ascribable to the residual PO_4^{3-} groups on the catalyst surface (i.e., in the form of Co-PO_4) rather than in the crystal lattice of the catalyst [42]. Finally, in the O 1s spectrum (Fig. 2e), the lattice hydroxyl peak at 530.9 eV emerged after alkaline HER, suggesting the formation of surface Co(OH)_2 , which was further confirmed by the XRD, Fourier transform infrared spectroscopy (FTIR), and Raman characterization studies of Fe-P-CMO after HER (as discussed below).

The changes in the XPS spectra of Fe-P-CMO were more dramatic after OER (Fig. 2). In the Co 2p spectrum (Fig. 2b), two new peaks appeared with binding energies being 780.1 and 795.1 eV (2:1 area ratio), typical of Co^{3+} in amorphous CoOOH [62]. No Mo signal was detected by XPS for Fe-P-CMO after OER (Fig. 2c), indicating the complete dissolution of Mo in the near surface region (top few nanometers) of the catalyst under the polarizing conditions of alkaline OER [42,43]. The Fe 2p spectrum after OER was almost unchanged (Fig. 2d), also confirming the stability of Fe_2O_3 under the polarizing conditions of alkaline OER in 1 M KOH. Signals due to P-O species in the O 1s (Fig. 2e) and P 2p (Fig. 2f) spectra of Fe-P-CMO almost disappeared after OER. The new signals for lattice oxygen (529.2 eV) [43] and lattice hydroxyl (531.1 eV) (Fig. 2e) appearing after alkaline OER implied the formation of surface CoOOH .

In summary, significant changes were seen in the elemental composition and metal speciation on the surface of Fe-P-CMO during HER and OER due to electrochemical reconstruction processes. The XRD pattern of Fe-P-CMO after HER is shown in Fig. 2g, showing diffraction peaks which could readily be attributed to Co(OH)_2 (PDF#02-0905), CoMoO_4 , and Fe_2O_3 . The emergence of Co(OH)_2 is associated with the transformation of Co^{2+} resulting from the dissolution of CoMoO_4 in 1 M KOH (i.e., $3\text{CoMoO}_4 + 2\text{H}_2\text{O} + 2\text{OH}^- \rightarrow 3\text{Co(OH)}_2 + \text{Mo}_3\text{O}_{10}^{2-}$) [32,42]. FTIR was applied to identify the formation of any hydroxyl phases after HER (Fig. S6). A sharp absorption peak at 3649 cm^{-1} appeared after HER, assigned to the O-H stretching vibration of non-hydrogen-bonded hydroxyl phases in Co(OH)_2 [41]. In contrast, the XRD pattern of Fe-P-CMO after OER (Fig. 2g,) showed only peaks due to NF and Fe_2O_3 , indicating that any new phases formed during OER, such as CoOOH , were amorphous [32,43]. The BET surface area of the reconstructed Fe-P-CMO catalyst increased by 15 times during HER relative to pristine Fe-P-CMO, implying more exposed active sites (Fig S6). Raman characterization studies were conducted to follow the compositional evolution of Fe-P-CMO during HER and OER (Fig. 2h.). The Raman spectrum of pristine Fe-P-CMO showed peaks due to Co-O-Mo ($\sim 346\text{ cm}^{-1}$),

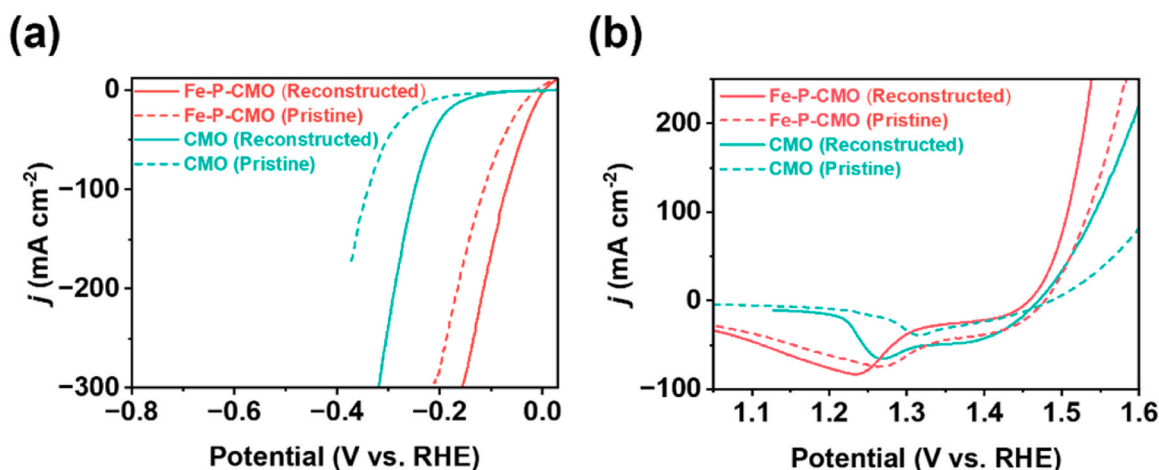


Fig. 3. (a) HER and (b) OER polarization curves for pristine and reconstructed Fe-P-CMO and CMO.

O–Mo–O (~ 810 , 870 , and 930 cm^{-1}), and Mo–O ($\sim 184\text{ cm}^{-1}$) vibrations of CoMoO_4 [41,42]. After HER, a new broad peak located at 533 cm^{-1} appeared due to Co(OH)_2 [32,42,63], whilst the characteristic peaks of CoMoO_4 became weaker due to the formation of surface Co(OH)_2 on P- CoMoO_4 . In the Raman spectrum of Fe-P-CMO after OER, the peaks due to CoMoO_4 had almost disappeared, whilst new peaks were observed at 512 and 660 cm^{-1} due to CoOOH [42], consistent with no molybdenum being found by XPS in the surface region of the catalyst after OER (Fig. 2c). Together with the XPS (Fig. 2e) and XRD (Fig. 2g) characterization data of Fe-P-CMO after OER, the data provided strong evidence for the transformation of CoMoO_4 to amorphous CoOOH during OER. Besides, the XRD pattern of CMO after OER (Fig. S8) confirmed the presence of amorphous CoOOH (PDF#26–0480), with the XPS signal for Mo in CMO almost disappearing after OER (Fig. S9a), further signifying the conversion of CoMoO_4 into CoOOH during OER. Results are consistent with a previous report, where a deep reconstruction of molybdate electrocatalysts was observed during alkaline OER [64]. Specifically, with co-leaching of crystal H_2O and MoO_4^{2-} in hydrated molybdates under electro-oxidation conditions, loose oxyhydroxide layers are formed on molybdates, allowing alkaline electrolyte penetration into the internal structures of molybdates, facilitating continuous co-leaching of crystal H_2O and MoO_4^{2-} , and eventually leading to the complete reconstruction of molybdates into oxyhydroxide phases [65]. Moreover, the abundant defects and voids in molybdates favor alkaline electrolyte penetration into the molybdate cores [66]. After alkaline OER using CMO, similar to the case of Fe-P-CMO, two new signals for lattice oxygen (529.1 eV) and lattice hydroxyl (531.2 eV) appeared (Fig. S9b), implying the formation of CoOOH [42]. Additionally, the Co 2p spectrum revealed the co-presence of Co^{3+} and Co^{2+} (Fig. S9c), also implying the formation of surface CoOOH [67]. X-band electron paramagnetic resonance (EPR) spectroscopy was next applied to verify that both thermal phosphorization and electrochemical oxidation reconstruction (during alkaline OER) could produce abundant OVs on the surface of catalysts [67]. EPR spectra of both CMO after OER and pristine Fe-P-CMO showed an intense signal at $g = 2.001$ associated with OVs (Fig. S10). The dramatically enhanced intensity of signal at $g = 2.001$ for CMO after OER relative to pristine CMO fully substantiated the generation of copious OVs on the surface of catalyst during alkaline OER. It has been well-established that OVs presented during HER and OER can act synergistically with active metal sites nearby in the catalyst, improve conductivity, and kinetically facilitate the adsorption of H_2O for HER or OH^- for OER as well as the desorption of H_2 or O_2 , respectively, from the electrocatalyst surface [68–70].

Electrochemical activity changes for the CMO and Fe-P-CMO catalysts, before and after reconstruction during OER and HER, were examined (Fig. 3a and b). As shown in Fig. 3a, the HER activity of CMO and Fe-P-CMO remarkably increased after reconstruction, with the required overpotentials to achieve a current density of 100 mA cm^{-2} decreasing by 92 mV for CMO and 47 mV for Fe-P-CMO. The chronoamperometry (CP) test for Fe-P-CMO at a cathodic current density of 100 mA cm^{-2} showed a pronounced enhancement of HER activity with time (Fig. S11). Notably, the significant decline in the amount of Mo^{4+} (Fig. 2c) appeared to enhance the HER activity, which proved that low-valence Mo species in Fe-P-CMO were not an important HER active site. A similar activity enhancement was observed during the OER (Fig. 3b).

The above analysis corroborated that the CoMoO_4 -based materials (CMO, P-CMO, and Fe-P-CMO) underwent electrochemical reconstruction during alkaline water electrolysis, with reconstruction leading to increased catalytic activity. During HER, CoMoO_4 -based materials only underwent surface reconstruction, resulting in the *in-situ* formation of Co(OH)_2 on the CoMoO_4 surface. Specifically, Fe-P-CMO reconstructed to form $\text{Fe}_2\text{O}_3/\text{Co(OH)}_2/\text{P-CoMoO}_4$, whilst P-CMO was transformed into $\text{Co(OH)}_2/\text{P-CoMoO}_4$ and CMO into $\text{Co(OH)}_2/\text{CoMoO}_4$. During alkaline OER, deep reconstruction occurred with the CoMoO_4 phase being completely converted into amorphous CoOOH . Specifically, Fe-P-CMO was reconstructed into $\text{Fe}_2\text{O}_3/\text{CoOOH}$, and P-CMO and CMO into

CoOOH . In summary, the leaching of Mo from CoMoO_4 into the electrolyte led to the *in-situ* production of Co(OH)_2 on NF during HER and CoOOH on NF during OER under alkaline conditions, where Mo served as a sacrificial agent to *in-situ* create these fresh active Co species, thereby boosting HER and OER activities.

3.3. HER performance

The HER performance of as-prepared catalysts was evaluated in 1 M KOH . As seen in the HER polarization curves (Fig. 4a), Fe-P-CMO required low overpotentials of 68 and 151 mV (vs. RHE) to achieve 100 and 300 mA cm^{-2} , respectively, the lowest amongst the electrocatalysts studied in this work. The polarization curves for Fe-P-CMO and P-CMO showed obvious reduction peaks at low potentials, which masked the true activity [71]. To determine the actual activity at low potentials, the polarization curves were scanned in the negative direction (shown by dashed lines in Fig. 4a). Combined with the CP test under 10 mA cm^{-2} in Fig. 4e, the HER overpotentials at 10 mA cm^{-2} were estimated to be ~ 10 and $\sim 32\text{ mV}$ for Fe-P-CMO and P-CMO, respectively. Real-time video data for the HER test of Fe-P-CMO are shown in Movie S1, in which the overpotential to drive 10 mA cm^{-2} could stabilize at $\sim 10\text{ mV}$ during the HER process. The activity trend in Fig. 4a of Fe-P-CMO > P-CMO > CMO certified that the introduction of Fe_2O_3 and the phosphorization treatment significantly enhanced the HER activity. For benchmarking purposes, we also recorded HER polarization curves for 20 wt\% Pt/C/NF , with the required overpotentials determined to be 9 , 109 , and 200 mV at 10 , 100 , and 300 mA cm^{-2} , respectively. Moreover, SEM images of 20 wt\% Pt/C coated on the NF (Fig. S12) showed that the loading of Pt/C particles was not uniform, which would result in unfavorable H_2 bubble adhesion/desorption. The HER activity of P-CFP was also studied (Fig. 4a), which was much lower than that of Fe-P-CMO, verifying that the $\text{Co}_3[\text{Fe(CN)}_6]_2$ formation on the CoMoO_4 surface during catalyst preparation played an important role in eventually achieving a high-HER efficiency on the Fe-P-CMO electrocatalyst. Fig. 4b shows HER Tafel plots derived from the polarization curves for the different catalysts. The Tafel slope for Fe-P-CMO (22.8 mV dec^{-1}) was substantially smaller than those determined for P-CMO (28.3 mV dec^{-1}), CMO (99.3 mV dec^{-1}), P-CFP (59.7 mV dec^{-1}), and Pt/C (44 mV dec^{-1}), implying a faster HER rate of Fe-P-CMO. The Tafel slopes of 22.8 and 28.3 mV dec^{-1} seen for Fe-P-CMO and P-CMO, respectively, suggested a conventional Volmer-Tafel mechanism, with the H_2 desorption (Tafel step) being the rate-determining step rather than the H_2O dissociation (Volmer step) [40]. Herein, non-metal oxygen sites (such as OVs/lattice oxygen) offer optimal H^* adsorption and H_2 desorption [11], thus accelerating the HER kinetics of P-CMO and Fe-P-CMO. Moreover, the exchange current density (j_0) was obtained by extrapolating the Tafel plots to zero overpotential (Fig. S13), which reflected the intrinsic electron transfer ability during electrocatalysis [11]. Fe-P-CMO offered a j_0 value of 2.664 mA cm^{-2} , approximately two-fold higher than that of P-CMO (1.315 mA cm^{-2}), which was attributed to the presence of the Fe_2O_3 phase in Fe-P-CMO. Further, the j_0 value of P-CMO was approximately five-fold higher than that of CMO, highlighting the vital roles of OVs and P-doping in enhancing the HER activity. Electrochemical impedance spectroscopy (EIS) Nyquist plots (Fig. 4c) established that Fe-P-CMO possessed a lower charge transfer resistance ($R_{ct} = 0.24\ \Omega$) compared to P-CMO ($0.8\ \Omega$), CMO ($17.4\ \Omega$), and P-CFP ($6\ \Omega$), implying its more efficient electron transfer during HER [40]. To estimate the electrochemically active surface areas (ECSA) of Fe-P-CMO, P-CMO, and CMO, their double-layer capacitances (C_{dl}) were estimated from CV curves collected at different scan rates in a non-Faradaic potential window (Fig. S14). As shown in Fig. 4d, the C_{dl} (11 mF cm^{-2}) for Fe-P-CMO was larger than that of P-CMO (9.2 mF cm^{-2}) and much larger than that of CMO (2.5 mF cm^{-2}), indicating Fe-P-CMO held higher surface roughness and offered more exposed active sites for HER. Furthermore, the intrinsic catalytic activity of each catalyst was estimated by normalizing the HER polarization curve against the ECSA

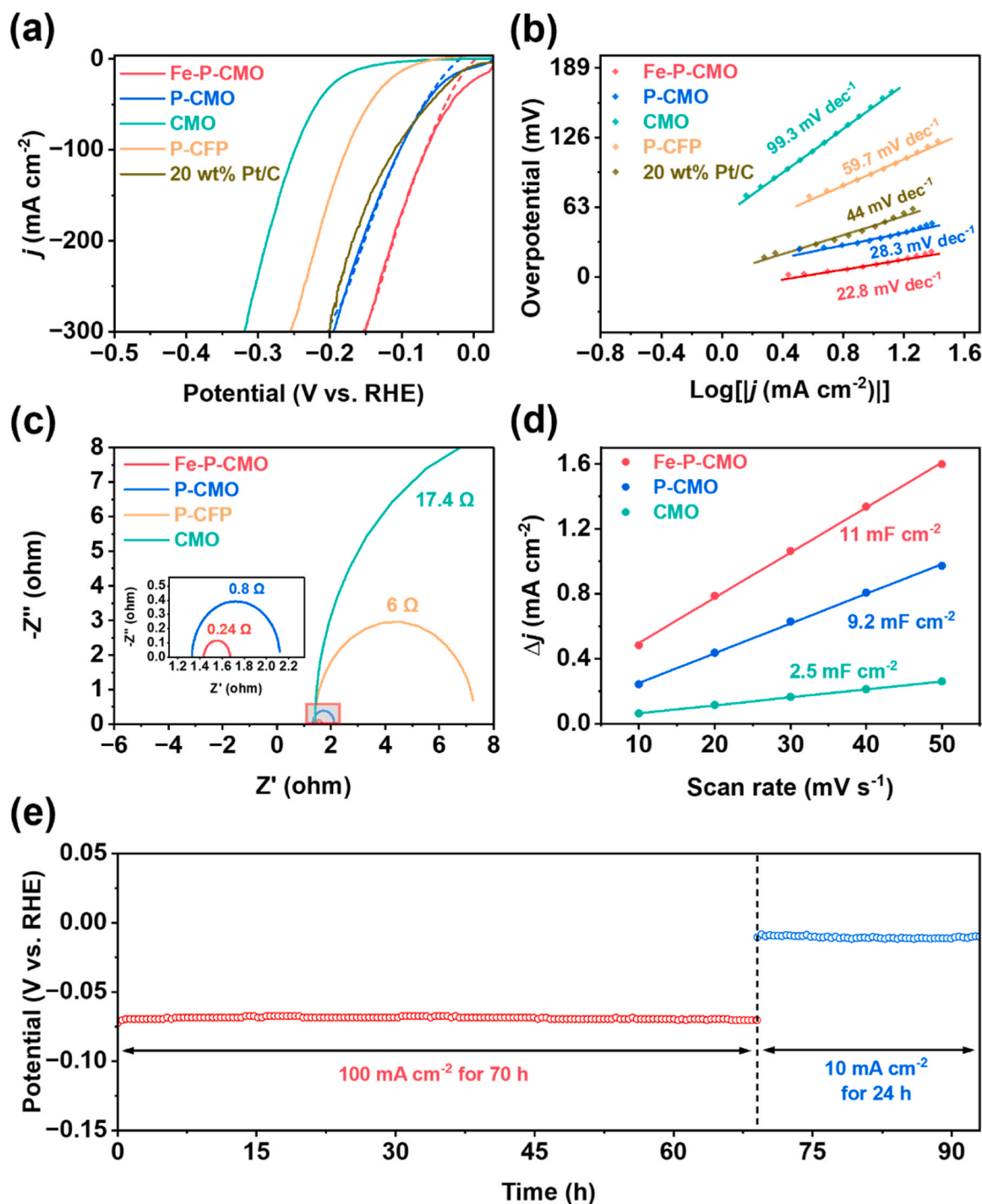


Fig. 4. HER performance of different catalysts in 1 M KOH. (a) Polarization curves, (b) Tafel slopes, (c) Nyquist plots, and (d) double-layer capacitances; (e) CP tests for Fe-P-CMO at different current densities.

value (Fig. S15), with the analysis revealing that Fe-P-CMO offered the optimum performance. The excellent stability of Fe-P-CMO was confirmed by the CP test at a constant current density of 100 mA cm⁻², with an increase of just 2 mV observed over 70 h. Subsequently, negligible change was observed at 10 mA cm⁻² over 24 h (Fig. 4e). It should be pointed out that the Fe-P-CMO composite had been subjected to a surface reconstruction treatment prior to the stability test and thus exhibited excellent stability without an abrupt enhancement of HER activity with time during initial HER (*i.e.*, surface reconstruction) as shown in Fig. S11. The surface reconstruction treatment prior to the stability test was also conducted toward the Fe-P-CMO composite

employed for the subsequent OER and overall water splitting. LSV curves for the Fe-P-CMO catalyst before and after stability tests almost overlapped, further implying outstanding catalyst stability during HER (Fig. S16).

Supplementary material related to this article can be found online at [doi:10.1016/j.apcatb.2024.123741](https://doi.org/10.1016/j.apcatb.2024.123741).

3.4. OER performance

Next, the OER abilities of Fe-P-CMO and the other reference electrocatalysts were evaluated to assess their bifunctional potentials for

water splitting. As shown in Fig. 5a for all OER polarization curves of these samples, large anodic peaks emanating from the oxidation of Co^{2+} appeared in polarization curves of CMO, P-CMO, and Fe-P-CMO containing Co^{2+} . In order to avoid the influence of the anodic peak, the overpotentials were obtained from polarization curves scanned in the negative direction [15,72,73]. The activity trend of Fe-P-CMO > CMO > P-CMO showed that the slightly weakened OER activity resulting from the phosphorization treatment of CMO was effectively countered by the introduction of Fe_2O_3 . A similar degradation in OER activity with phosphorization was also reported by Xiao and co-workers [43], but the underlying reasons were not discussed. Considering the deep

reconstruction of catalysts that occurred during OER (i.e., dissolution of Mo and P, and formation of CoOOH), we proposed that the weakened OER performance of P-CMO with respect to CMO related to the nature of the OV-CoOOH active phase formed by electro-oxidation for each catalyst, while the CoOOH phase formed from P-CMO had a lower Co^{3+} content (Fig. S17) which adversely impacted OER [74]. Less Co^{3+} might have been the result of increased OVs generated by the phosphorization treatment. As shown in Fig. 5b, the overpotentials required to achieve current densities of 10 and 200 mA cm^{-2} for Fe-P-CMO were 238 and 304 mV, respectively, much smaller than the corresponding values for CMO (251 and 361 mV), P-CMO (264 and 374 mV), and P-CFP (254 and

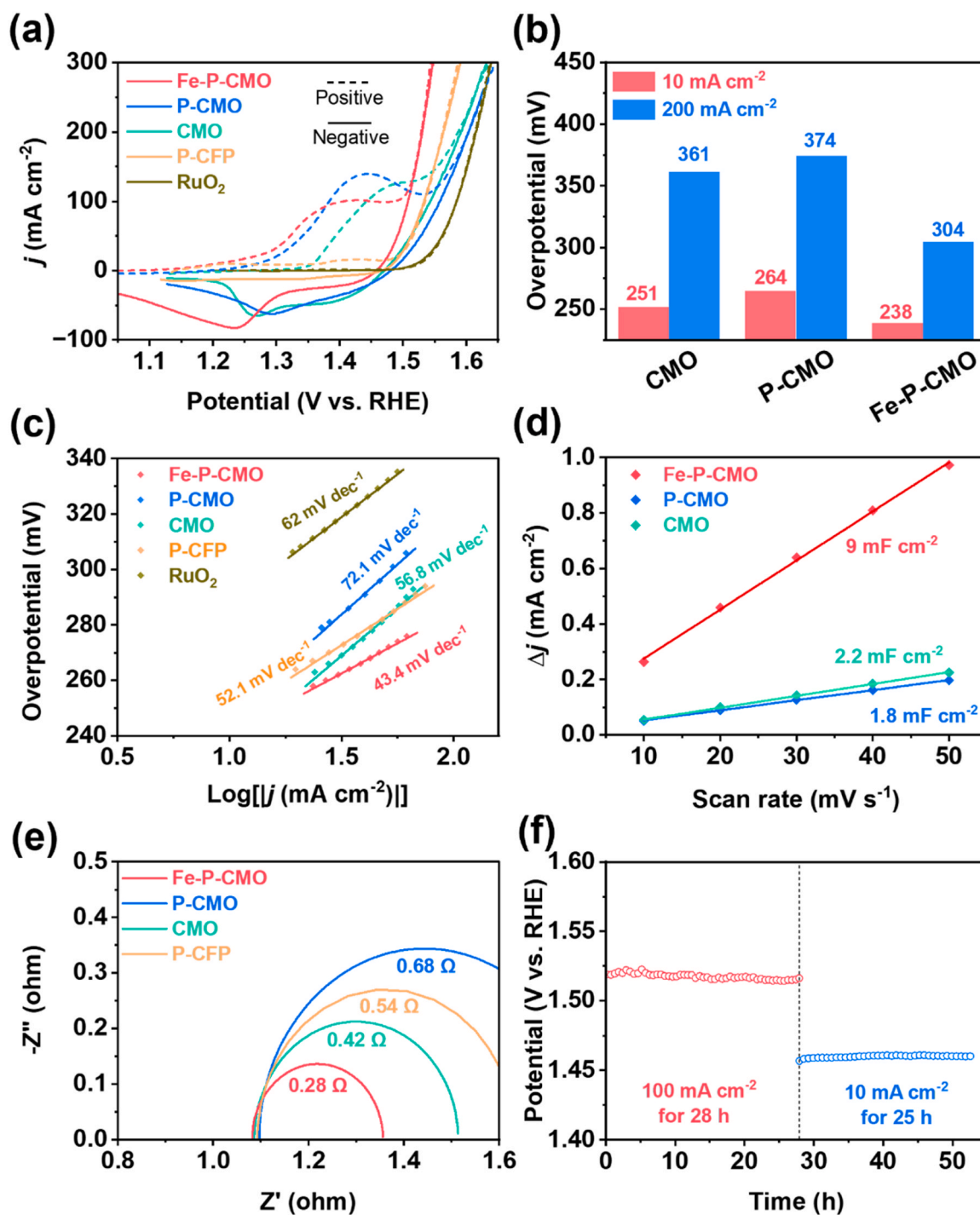


Fig. 5. OER performance of different catalysts in 1 M KOH. (a) Polarization curves, (b) comparative η_{10} and η_{200} values, (c) Tafel slopes, (d) double-layer capacitances, and (e) Nyquist plots; (f) CP tests for Fe-P-CMO under different current densities.

334 mV). Further, Fe-P-CMO outperformed RuO₂ (293 and 385 mV), a benchmark OER catalyst. The data demonstrated that the introduction of Fe₂O₃ greatly improved the OER activity, especially at high current densities. As shown in Fig. 5c, Fe-P-CMO offered a low OER Tafel slope of just 43.4 mV dec⁻¹, much lower than those determined for CMO (56.8 mV dec⁻¹), P-CMO (72.1 mV dec⁻¹), P-CFP (52.1 mV dec⁻¹), and commercial RuO₂ (49.8 mV dec⁻¹), confirming faster OER kinetics. In addition, the value of 43.4 mV dec⁻¹ determined for Fe-P-CMO was close to 40 mV dec⁻¹, suggesting the rate-determining step for OER was the second electron transfer step [6], i.e., $\text{OH}^- + \text{OH}^* \rightarrow \text{H}_2\text{O} + \text{O}^* + \text{e}^-$. As shown in Fig. 5d, the C_{dl} determined from CV curves collected at different scan rates in a non-Faradaic potential window (Fig. S18) increased linearly with the scan rate, with values of 9, 1.8, and 2.2 mF cm⁻² determined for Fe-P-CMO, P-CMO, and CMO, respectively. Results indicated that Fe-P-CMO possessed a higher surface roughness and more exposed active sites for OER. EIS Nyquist plots (Fig. 5e) showed that the R_{ct} value for Fe-P-CMO (0.28 Ω) was smaller than those determined for P-CMO (0.68 Ω), CMO (0.42 Ω), and P-CFP (0.54 Ω), suggesting rapid charge-transfer between Fe-P-CMO and surface adsorbed species during OER. The durability of Fe-P-CMO during the OER process was tested at constant current densities of 10 mA cm⁻² for 25 h and 100 mA cm⁻² for 28 h, with negligible degradation in the catalyst performance observed (Fig. 5f).

To summarize, the introduction of Fe₂O₃ increased the ECSA of Fe-P-

CMO several times relative to P-CMO and CMO and accelerated electron transfer, thus significantly boosting the OER activity. The data demonstrated that Fe₂O₃ served as a crucial OER-promoting component in Fe-P-CMO.

3.5. Overall water splitting performance

Owing to its excellent HER activity and good OER activity, the self-supporting Fe-P-CMO electrode was directly used as both the cathode and the anode to establish an alkaline water splitting cell (Fig. 6a). The electrolyte was 1 M KOH. Movie S2 shows the actual cell system, in which large amounts of gas bubbles were continuously produced at both electrodes. Fig. 6b compares the performance of the Fe-P-CMO (-) || Fe-P-CMO (+) system with a benchmark Pt/C (-) || RuO₂ (+) system. The Fe-P-CMO (-) || Fe-P-CMO (+) system required only 1.59 V to maintain a current density of 100 mA cm⁻². A clear oxidation peak was observed over 1.2 – 1.5 V in the polarization curve collected in the positive direction for the Fe-P-CMO (-) || Fe-P-CMO (+) full cell, masking the true activity. Accordingly, the polarization curve was scanned in negative direction (red dotted line in Fig. S19a), revealing that the true required cell voltage needed to maintain 10 mA cm⁻² was only 1.48 V. For the Pt/C (-) || RuO₂ (+) full cell, cell voltages of 1.56 and 1.75 V were required to achieve 10 and 100 mA cm⁻², respectively. Fig. 6c shows CP data for the Fe-P-CMO (-) || Fe-P-CMO (+) system at 100 mA cm⁻² for

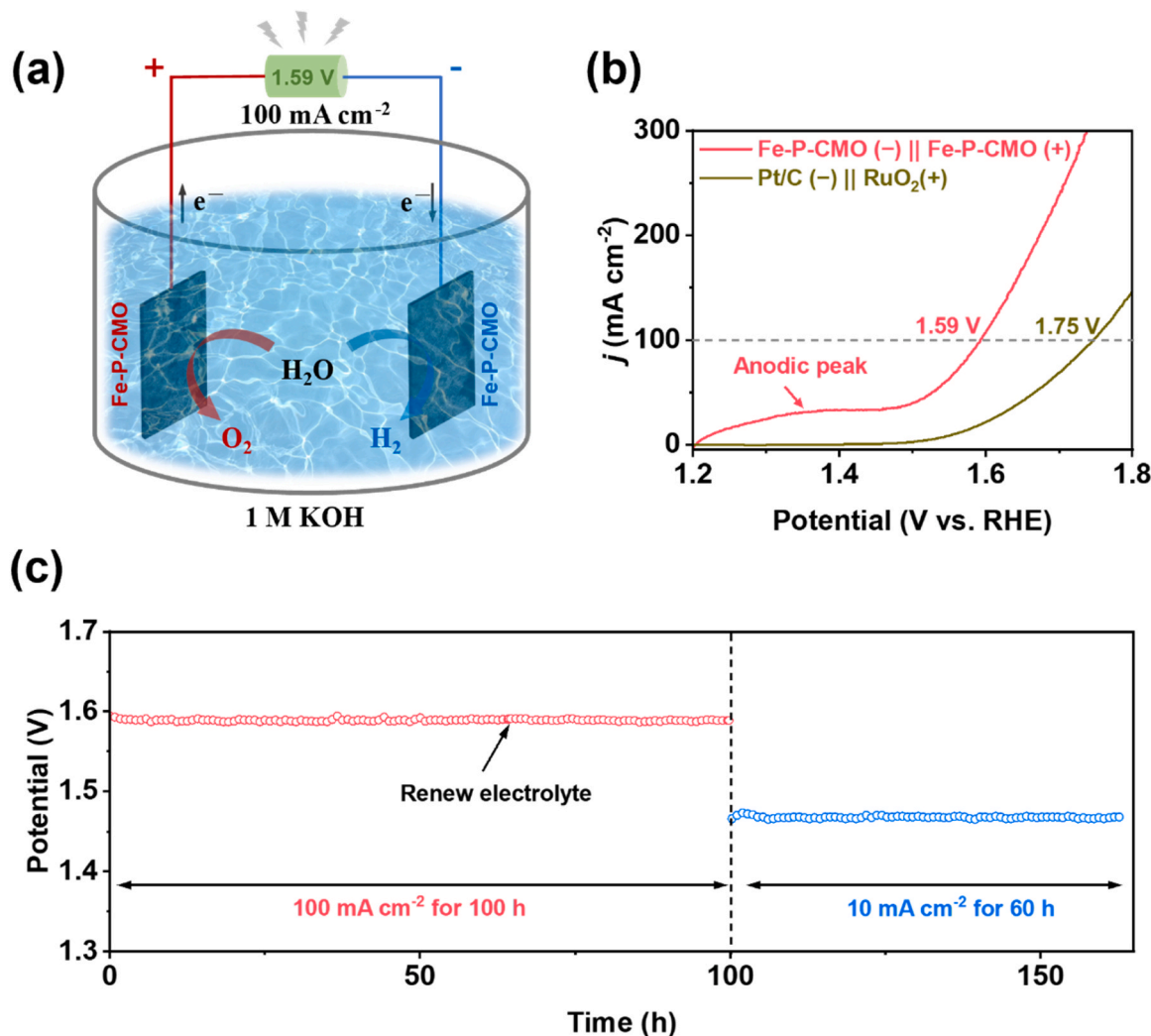


Fig. 6. (a) Schematic diagram of Fe-P-CMO (-) || Fe-P-CMO (+) cell system, (b) polarization curves of Fe-P-CMO (-) || Fe-P-CMO (+) and Pt/C (-) || RuO₂ (+) cell systems, and (c) CP tests at different current densities of the Fe-P-CMO (-) || Fe-P-CMO (+) cell system.

100 h and then 10 mA cm⁻² for 60 h. Negligible activity degradation occurred, verifying the excellent stability of the Fe-P-CMO (–) || Fe-P-CMO (+) system for overall water splitting. Notably, no activity degradation occurred when the electrolyte was renewed after operation of this cell for 65 h, suggesting that the leaching/dissolution of Mo into the electrolyte during HER and OER did not adversely affect these two reactions. After the stability tests, the polarization curve was recorded to further confirm the excellent stability of the Fe-P-CMO (–) || Fe-P-CMO (+) system (Fig. S19b). As expected, the LSV profiles collected before and after the stability tests almost overlapped perfectly. The overall water splitting performance of our Fe-P-CMO (–) || Fe-P-CMO (+) system ranks among the best full cell systems employing bifunctional OER/HER catalysts recently reported (Table S1).

Supplementary material related to this article can be found online at [doi:10.1016/j.apcatb.2024.123741](https://doi.org/10.1016/j.apcatb.2024.123741).

Density functional theory (DFT) calculations were performed using the Vienna Ab initio Simulation Package (VASP) to gain a better understanding of the water splitting mechanism on Fe-P-CMO. It was hypothesized that P-doped CoMoO₄ (P-CMO) provided active sites for the alkaline water splitting. Accordingly, the P-CMO model was established and optimized as presented in Fig. S20a. Under alkaline conditions, the HER proceeds via four elemental reaction steps, that is, the adsorption of a water molecule, the breakage of H–OH bond, the desorption of *OH, and the desorption of H₂. The intermediates (*i.e.*, *H₂O, *H + *OH, and *H) involved in alkaline HER on P-CMO were also optimized (Fig. S20b–d). Subsequently, the Gibbs free energy diagram for alkaline HER on P-CMO was calculated and depicted in Fig. S20e. Clearly, the desorption of *OH showed the largest energy barrier up to 1.23 eV, thus representing the rate-determining step (RDS) in the alkaline HER. Regarding the alkaline OER, the four-electron pathway involved four intermediates including *OH, *O, *OOH, and *O₂ as shown in Fig. S21a–d, respectively. Similarly, the Gibbs free energy diagram for alkaline OER on P-CMO was further calculated and illustrated in Fig. S21e. It was found that the formation of *OOH was the most endothermic step, being the RDS with an energy barrier of 2.90 eV. Differential charge density calculations were performed for CMO and P-CMO to probe into the change of electronic structure of CoMoO₄ after P incorporation (Fig. S22). It could be seen that the P dopant was able to donate electrons to CoMoO₄. The charge transferred from each P dopant atom to CoMoO₄ was as high as 0.93 e⁻ according to Bader charge analysis. Such an electron transfer effect was beneficial to increase the reactivity of Co sites on the surface for water splitting.

4. Conclusions

In this work, a novel Fe-P-CMO electrocatalyst was successfully developed for overall water splitting. The catalyst consisted of Fe₂O₃/P-doped CoMoO₄ heterojunctions on NF. It was found that both thermal phosphorization step and electrochemical oxidation reconstruction for CoMoO₄ (during alkaline OER) produced abundant OV's on the surface of catalysts. During alkaline OER, the P-doped CoMoO₄ underwent deep reconstruction to form CoOOH, resulting in a Fe₂O₃/CoOOH active phases. The active phase for HER was determined to be Fe₂O₃/Co(OH)₂/P-CoMoO₄. The highly heterogeneous structure Fe₂O₃/Co(OH)₂/P-CoMoO₄ acted to increase the electron transfer rate kinetics and intrinsic electrochemical activity, greatly enhancing HER kinetics. A Fe-P-CMO (–) || Fe-P-CMO (+) full cell water splitting system (1 M KOH) offered excellent stability at 100 mA cm⁻² for 100 h followed by 10 mA cm⁻² for 60 h, with a cell voltages of 1.48 V and 1.59 V required to maintain current densities of 10 and 100 mA cm⁻², respectively. Fe-P-CMO represents one of the best bifunctional catalysts reported to date for alkaline water splitting.

CRedit authorship contribution statement

He Yingjian: Formal analysis, Investigation, Methodology. **Liu Qin:**

Investigation, Visualization. **Kennedy John V.:** Formal analysis. **Li Junhua:** Formal analysis. **Zhang Xinxin:** Investigation, Validation. **Luo Ziyu:** Formal analysis. **Waterhouse Geoffrey I. N.:** Conceptualization, Formal analysis, Writing – review & editing. **Wang Bowen:** Data curation, Formal analysis, Investigation, Methodology. **Qian Dong:** Conceptualization, Formal analysis, Project administration, Supervision, Writing – original draft. **Liu Jinlong:** Conceptualization, Formal analysis, Software. **Chen Xiangxiang:** Data curation, Formal analysis, Investigation, Methodology.

Declaration of Competing Interest

The authors declare that they have no known competing financial interests or personal relationships that could have appeared to influence the work reported in this paper.

Data Availability

Data will be made available on request.

Acknowledgements

This work was financially supported by National Natural Science Foundation of China (No. 51874359, 52103354, 21171174 and 21505035), the Natural Science Foundation of Hunan Province (2022JJ20084), the Science and Technology Innovation Program of Hunan Province (2023RC3034), and Research Faculty Startup Funding of Central South University (202045020). GINW acknowledges funding support from the Royal Society Te Aparangi (*via* award of a James Cook Research Fellowship), the New Zealand Ministry of Business, Innovation and Employment (MBIE, contract C05×2007, Aotearoa: Green Hydrogen Technology Platform), and a philanthropic donation from Greg and Kathryn Trounson. Also, we are grateful to the High Performance Computing Centre of Central South University for assistance with the computations.

Appendix A. Supporting information

Supplementary data associated with this article can be found in the online version at [doi:10.1016/j.apcatb.2024.123741](https://doi.org/10.1016/j.apcatb.2024.123741).

References

- [1] Y. Wang, X.P. Li, Z. Huang, H.Z. Wang, Z.L. Chen, J.F. Zhang, X.R. Zheng, Y. D. Deng, W.B. Hu, Amorphous Mo-doped Ni₅₀Se_{0.5} nanosheets@crystalline Ni_{50.5}Se_{0.5} nanorods for high current-density electrocatalytic water splitting in neutral media, *Angew. Chem. Int. Ed.* 62 (2023) e202215256.
- [2] H.M. Wang, Z.N. Chen, D.S. Wu, M.N. Cao, F.F. Sun, H. Zhang, H.H. You, W. Zhuang, R. Cao, Significantly enhanced overall water splitting performance by partial oxidation of Ir through Au modification in core-shell alloy structure, *J. Am. Chem. Soc.* 143 (2021) 4639–4645.
- [3] N.S. Gultom, T.S. Chen, M.Z. Silitonga, D.H. Kuo, Overall water splitting realized by overall sputtering thin-film technology for a bifunctional MoNiFe electrode: a green technology for green hydrogen, *Appl. Catal. B: Environ.* 322 (2023) 122103.
- [4] C. Liu, X. Chen, X. Zhang, J. Li, B. Wang, Z. Luo, J. Li, D. Qian, J. Liu, G.I. N. Waterhouse, Sodium tartrate-assisted synthesis of high-purity NiFe₂O₄ nanomicrospheres supported by porous ketjenblack carbon for efficient alkaline oxygen evolution, *J. Phys. Chem. Lett.* 14 (2023) 6099–6109.
- [5] Z.Z. Zhu, K. Xu, W. Guo, H.Y. Zhang, X. Xiao, M.S. He, T.T. Yu, H. Zhao, D. E. Zhang, T. Yang, Vanadium-phosphorus incorporation induced interfacial modification on cobalt catalyst and its super electrocatalysis for water splitting in alkaline media, *Appl. Catal. B: Environ.* 304 (2022) 120985.
- [6] X. Long, B. Wang, X. Zhang, X. Mao, J. Li, Z. Luo, D. Qian, J. Li, J. Liu, Disruptive strategy to fabricate three-dimensional ultrawide interlayer porous carbon framework-supported Prussian blue nanocubes: a carrier for NiFe-layered double-hydroxide toward oxygen evolution, *Inorg. Chem.* 61 (2022) 19624–19632.
- [7] J. Guo, J. Liu, X. Mao, S. Chu, X. Zhang, Z. Luo, J. Li, B. Wang, C. Jia, D. Qian, Experimental and theoretical insights into enhanced hydrogen evolution over PtCo nanoalloys anchored on a nitrogen-doped carbon matrix, *J. Phys. Chem. Lett.* 13 (2022) 5195–5203.
- [8] J. Zhu, L.S. Hu, P.X. Zhao, L.Y.S. Lee, K.Y. Wong, Recent advances in electrocatalytic hydrogen evolution using nanoparticles, *Chem. Rev.* 120 (2020) 851–918.

- [9] J. Ren, Q. Wang, Q. Xiang, C. Yang, Y. Liang, J. Li, J. Liu, D. Qian, O-vacancy-rich and heterostructured Cu/Cu₂O/NiO@NiCu foam self-supported advanced electrocatalyst towards hydrogen evolution: an experimental and DFT study, *Chem. Eng. Sci.* 280 (2023) 119026.
- [10] L. Cao, Q. Luo, W. Liu, Y. Lin, X. Liu, Y. Cao, W. Zhang, Y. Wu, J. Yang, T. Yao, S. Wei, Identification of single-atom active sites in carbon-based cobalt catalysts during electrocatalytic hydrogen evolution, *Nat. Catal.* 2 (2019) 134–141.
- [11] J. Dai, Y.L. Zhu, H.A. Tahini, Q. Lin, Y. Chen, D.Q. Guan, C. Zhou, Z.W. Hu, H. J. Lin, T.S. Chan, C.T. Chen, S.C. Smith, H.T. Wang, W. Zhou, Z.P. Shao, Single-phase perovskite oxide with super-exchange induced atomic-scale synergistic active centers enables ultrafast hydrogen evolution, *Nat. Commun.* 11 (2020) 5657.
- [12] R. Subbaraman, D. Tripkovic, D. Strmcnik, K.C. Chang, M. Uchiumura, A. P. Paulikas, V. Stamenkovic, N.M. Markovic, Enhancing hydrogen evolution activity in water splitting by tailoring Li⁺-Ni(OH)₂-Pt interfaces, *Science* 334 (2011) 1256–1260.
- [13] Z.W. Seh, J. Kibsgaard, C.F. Dickens, I.B. Chorkendorff, J.K. Nørskov, T. F. Jaramillo, Combining theory and experiment in electrocatalysis: Insights into materials design, *Science* 355 (2017) eaad4998.
- [14] D. Kim, Y. Lee, M. Kim, G. Lee, S.M.N. Jeghan, Designing a smart heterojunction coupling of cobalt-iron layered double hydroxide on nickel selenide nanosheets for highly efficient overall water splitting kinetics, *Appl. Catal. B: Environ.* 308 (2022) 121221.
- [15] C.-F. Li, J.-W. Zhao, L.-J. Xie, J.-Q. Wu, G.-R. Li, Fe doping and oxygen vacancy modulated Fe-Ni₃P₄/NiFeOH nanosheets as bifunctional electrocatalysts for efficient overall water splitting, *Appl. Catal. B: Environ.* 291 (2021) 119987.
- [16] S. Roy, D. Bagchi, L. Dheer, S.C. Sarma, V. Rajaji, C. Narayana, U.V. Waghmare, S. C. Peter, Mechanistic insights into the promotional effect of Ni substitution in non-noble metal carbides for highly enhanced water splitting, *Appl. Catal. B: Environ.* 298 (2021) 120560.
- [17] T. Gu, R. Sa, L. Zhang, D.-S. Li, R. Wang, Engineering interfacial coupling between Mo₂C nanosheets and Co@NC polyhedron for boosting electrocatalytic water splitting and zinc-air batteries, *Appl. Catal. B: Environ.* 296 (2021) 120360.
- [18] C.F. Li, J.W. Zhao, L.J. Xie, J.Q. Wu, G.R. Li, Water adsorption and dissociation promoted by Co²⁺-N-C^{*}-biactive sites of metallic Co/N-doped carbon hybrids for efficient hydrogen evolution, *Appl. Catal. B: Environ.* 282 (2021) 119463.
- [19] X. Yang, Z. Zhou, Y. Zou, J. Kuang, D. Ye, S. Zhang, Q. Gao, S. Yang, X. Cai, Y. Fang, Interface reinforced 2D/2D heterostructure of Cu-Co oxides/FeCo hydroxides as monolithic multifunctional catalysts for rechargeable/flexible zinc-air batteries and self-powered water splitting, *Appl. Catal. B: Environ.* 325 (2023) 122332.
- [20] S. Ramakrishnan, D.B. Velusamy, S. Sengodan, G. Nagaraju, D.H. Kim, A.R. Kim, D. J. Yoo, Rational design of multifunctional electrocatalyst: An approach towards efficient overall water splitting and rechargeable flexible solid-state zinc-air battery, *Appl. Catal. B: Environ.* 300 (2022) 120752.
- [21] Q. Wang, H. Xu, X.Y. Qian, G.Y. He, H.Q. Chen, Sulfur vacancies engineered self-supported Co₃S₄ nanoflowers as an efficient bifunctional catalyst for electrochemical water splitting, *Appl. Catal. B: Environ.* 322 (2023) 122104.
- [22] M. Ma, J. Xu, H. Wang, X. Zhang, S. Hu, W. Zhou, H. Liu, Multi-interfacial engineering of hierarchical CoNi₂S₄/WS₂/Co₃S₈ hybrid frameworks for robust all-pH electrocatalytic hydrogen evolution, *Appl. Catal. B: Environ.* 297 (2021) 120455.
- [23] M. Batool, A. Hameed, M.A. Nadeem, Recent developments on iron and nickel-based transition metal nitrides for overall water splitting: A critical review, *Coord. Chem. Rev.* 480 (2023) 215029.
- [24] A. Li, L. Zhang, F. Wang, L. Zhang, L. Li, H. Chen, Z. Wei, Rational design of porous Ni-Co-Fe ternary metal phosphides nanobricks as bifunctional electrocatalysts for efficient overall water splitting, *Appl. Catal. B: Environ.* 310 (2022) 121353.
- [25] C.L. Huang, Y.G. Lin, C.L. Chiang, C.K. Peng, D.S. Raja, C.T. Hsieh, Y.A. Chen, S. Q. Chang, Y.X. Yeh, S.Y. Lu, Atomic scale synergistic interactions lead to breakthrough catalysts for electrocatalytic water splitting, *Appl. Catal. B: Environ.* 320 (2023) 122016.
- [26] K. Harish, J. Balamurugan, T.T. Nguyen, N.H. Kim, J.H. Lee, Advanced interfacial engineering of oxygen-enriched Fe_xSn_{1-x}OSe nanostructures for efficient overall water splitting and flexible zinc-air batteries, *Appl. Catal. B: Environ.* 305 (2022) 120924.
- [27] W. Zou, C. Sun, K. Zhao, J. Li, X. Pan, D. Ye, Y. Xie, W. Xu, H. Zhao, L. Zhang, J. Zhang, Surface reconstruction of NiCoP pre-catalysts for bifunctional water splitting in alkaline electrolyte, *Electrochim. Acta* 345 (2020) 136114.
- [28] T.Z. Xiong, B.W. Huang, J.J. Wei, X.C. Yao, R. Xiao, Z.X. Zhu, F. Yang, Y.C. Huang, H. Yang, M.S. Balogun, Unveiling the promotion of accelerated water dissociation kinetics on the hydrogen evolution catalysis of NiMoO₄ nanorods, *J. Energy Chem.* 67 (2022) 805–813.
- [29] L.-J. Xie, C.-F. Li, J.-W. Zhao, L.-F. Gu, J.-Q. Wu, Y. Wang, G.-R. Li, Incorporating metal Co into CoMoO₄/Co₂Mo₃O₉ heterointerfaces with rich-oxygen vacancies for efficient hydrogen evolution catalysis, *Chem. Eng. J.* 430 (2022) 133119.
- [30] L.L. Guo, J.Q. Chi, J.W. Zhu, T. Cui, J.P. Lai, L. Wang, Dual-doping NiMoO₄ with multi-channel structure enable urea-assisted energy-saving H₂ production at large current density in alkaline seawater, *Appl. Catal. B: Environ.* 320 (2023) 121977.
- [31] J.T. Ren, X.M. Wu, T. Liu, L. Chen, R. Hao, Y.J. Song, Y.P. Liu, Z.Y. Yuan, Interfacing nickel with molybdenum oxides as monolithic catalyst to accelerate alkaline hydrogen electrocatalysis with robust stability, *Appl. Catal. B: Environ.* 317 (2022) 121786.
- [32] X. Cui, Y. Cui, M.L. Chen, R. Xiong, Y.C. Huang, X.W. Liu, Enhancing electrochemical hydrogen evolution performance of CoMoO₄-based microrod arrays in neutral media through alkaline activation, *ACS Appl. Mater. Interfaces* 12 (2020) 30905–30914.
- [33] J. Luo, W.H. Guo, Q. Zhang, X.H. Wang, L. Shen, H.C. Fu, L.L. Wu, X.H. Chen, H. Q. Luo, N.B. Li, One-pot synthesis of Mn-Fe bimetallic oxide heterostructures as bifunctional electrodes for efficient overall water splitting, *Nanoscale* 12 (2020) 19992–20001.
- [34] V.H. Nguyen, C. Lamie, J.J. Shim, Hierarchical mesoporous graphene@Ni-Co-S arrays on nickel foam for high-performance supercapacitors, *Electrochim. Acta* 161 (2015) 351–357.
- [35] B.A. Zhang, Z.Q. Jiang, X.N. Shang, S.S. Li, Z.J. Jiang, Accelerated hydrogen evolution reaction in Ni₃P/MoP₂/MoO₂ tri-phase composites with rich crystalline interfaces and oxygen vacancies achieved by plasma assisted phosphorization, *J. Mater. Chem. A* 9 (2021) 25934–25943.
- [36] M. Yang, Y. Jiang, M. Qu, Y. Qin, Y. Wang, W. Shen, R. He, W. Su, M. Li, Strong electronic couple engineering of transition metal phosphides-oxides heterostructures as multifunctional electrocatalyst for hydrogen production, *Appl. Catal. B: Environ.* 269 (2020) 118803.
- [37] F. Wang, K. Ma, W. Tian, J. Dong, H. Han, H. Wang, K. Deng, H. Yue, Y.X. Zhang, W. Jiang, J. Ji, P-Doped NiMoO₄ parallel arrays anchored on cobalt carbonate hydroxide with oxygen vacancies and mass transfer channels for supercapacitors and oxygen evolution, *J. Mater. Chem. A* 7 (2019) 19589–19596.
- [38] Y. Tang, C.H. Yang, X.T. Xu, Y.Q. Kang, J. Henzie, W.X. Que, Y. Yamauchi, MXene nanoarchitectonics: defect-engineered 2D MXenes towards enhanced electrochemical water splitting, *Adv. Energy Mater.* 12 (2022) 2103867.
- [39] Z. Wu, T. Liao, S. Wang, J.A. Mudiyansele, A.S. Micallef, W. Li, A.P. O'Mullane, J. Yang, W. Luo, K. Ostrikov, Y. Gu, Z. Sun, Conversion of catalytically inert 2D bismuth oxide nanosheets for effective electrochemical hydrogen evolution reaction catalysis via oxygen vacancy concentration modulation, *Nano-Micro Lett.* 14 (2022) 90.
- [40] Z. Xiao, M. Yang, J. Wang, Z. Xu, S. Zhang, A. Tang, R. Gao, H. Yang, FeNiP/MoO_x integrated electrode grown on monocrystalline NiMoO₄ nanorods with multi-interface for accelerating alkaline hydrogen evolution reaction, *Appl. Catal. B: Environ.* 303 (2022) 120913.
- [41] Z. Xiao, M. Yang, C. Liu, B. Wang, S. Zhang, J. Liu, Z. Xu, R. Gao, J.-J. Zou, A. Tang, H. Yang, Artificial modulated Lewis pairs for highly efficient alkaline hydrogen production, *Nano Energy* 98 (2022) 107233.
- [42] J. Wang, J. Hu, C. Liang, L. Chang, Y. Du, X. Han, J. Sun, P. Xu, Surface reconstruction of phosphorus-doped cobalt molybdate microarrays in electrochemical water splitting, *Chem. Eng. J.* 446 (2022) 137094.
- [43] Z. Xiao, J. Wang, C. Liu, B. Wang, Q. Zhang, Z. Xu, M.T. Sarwar, A. Tang, H. Yang, In-situ surface structural reconstruction of NiMoO₄ for efficient overall water splitting, *Appl. Surf. Sci.* 602 (2022) 154314.
- [44] Y. Zhang, L. Gao, E.J.M. Hensen, J.P. Hofmann, Evaluating the stability of Co₂P electrocatalysts in the hydrogen evolution reaction for both acidic and alkaline electrolytes, *ACS Energy Lett.* 3 (2018) 1360–1365.
- [45] W. Zhang, N. Han, J. Luo, X. Han, S. Feng, W. Guo, S. Xie, Z. Zhou, P. Subramanian, K. Wan, J. Arbiol, C. Zhang, S. Liu, M. Xu, X. Zhang, J. Fransaer, Critical role of phosphorus in hollow structures cobalt-based phosphides as bifunctional catalysts for water splitting, *Small* 18 (2022) e2103561.
- [46] W. Xie, J. Huang, L. Huang, S. Geng, S. Song, P. Tsiakaras, Y. Wang, Novel fluorine-doped cobalt molybdate nanosheets with enriched oxygen-vacancies for improved oxygen evolution reaction activity, *Appl. Catal. B: Environ.* 303 (2022) 120871.
- [47] J. Choi, D. Kim, W.R. Zheng, B.Y. Yan, Y. Li, L.Y.S. Lee, Y. Piao, Interface engineered NiFe₂O_{4-x}/NiMoO₄ nanowire arrays for electrochemical oxygen evolution, *Appl. Catal. B: Environ.* 286 (2021) 119857.
- [48] W. Shi, J. Zhu, L. Gong, D. Feng, Q. Ma, J. Yu, H. Tang, Y. Zhao, S. Mu, Fe-incorporated Ni/MoO₂ hollow heterostructure nanorod arrays for high-efficiency overall water splitting in alkaline and seawater media, *Small* 18 (2022) e2205683.
- [49] P.L. Sun, Y.T. Zhou, H.Y. Li, H. Zhang, L.G. Peng, Q.E. Cao, S.X. Liu, T. Waberg, G. Z. Hu, Round-the-clock bifunctional honeycomb-like nitrogen-doped carbon-decorated Co₂P/Mo₂C-heterojunction electrocatalyst for direct water splitting with 18.1% STH efficiency, *Appl. Catal. B: Environ.* 310 (2022) 121354.
- [50] X.T. Han, C. Yu, S. Zhou, C.T. Zhao, H.W. Huang, J. Yang, Z.B. Liu, J.J. Zhao, J. S. Qiu, Ultrasensitive iron-triggered nanosized Fe-CoOOH integrated with graphene for highly efficient oxygen evolution, *Adv. Energy Mater.* 7 (2017) 1602148.
- [51] W.H. Lee, M.H. Han, Y.J. Ko, B.K. Min, K.H. Chae, H.S. Oh, Electrode reconstruction strategy for oxygen evolution reaction: maintaining Fe-CoOOH phase with intermediate-spin state during electrolysis, *Nat. Commun.* 13 (2022) 605.
- [52] Y. Zhao, N. Dongfang, C.A. Triana, C. Huang, R. Erni, W. Wan, J. Li, D. Stoian, L. Pan, P. Zhang, J. Lan, M. Iannuzzi, G.R. Patzke, Dynamics and control of active sites in hierarchically nanostructured cobalt phosphide/chalcogenide-based electrocatalysts for water splitting, *Energy Environ. Sci.* 15 (2022) 727–739.
- [53] X.L. Lin, J.L. Liu, X.Q. Qiu, B.W. Liu, X.F. Wang, L.H. Chen, Y.L. Qin, Ru-FeNi alloy heterojunctions on lignin-derived carbon as bifunctional electrocatalysts for efficient overall water splitting, *Angew. Chem. Int. Ed.* 62 (2023) e202306333.
- [54] J.T. Ren, L. Chen, H.Y. Wang, W.W. Tian, X.L. Song, Q.H. Kong, Z.Y. Yuan, Synergistic activation of crystalline Ni₂P and amorphous NiMoO_x for efficient water splitting at high current densities, *ACS Catal.* 13 (2023) 9792–9805.
- [55] X.Y. Wang, X.Q. Xu, Y. Nie, R.H. Wang, J.L. Zou, Electronic-state modulation of metallic Co-assisted Co₇Fe₃ alloy heterostructure for highly efficient and stable overall water splitting, *Adv. Sci.* 10 (2023) 2301961.
- [56] L.M. Cao, Y.W. Hu, S.F. Tang, A. Iljin, J.W. Wang, Z.M. Zhang, T.B. Lu, Fe-CoP electrocatalyst derived from a bimetallic Prussian blue analogue for large-current-density oxygen evolution and overall water splitting, *Adv. Sci.* 5 (2018) 1800949.

- [57] P. Wang, X. Li, S. Fan, Z. Yin, L. Wang, M.O. Tadé, S. Liu, Piezotronic effect and oxygen vacancies boosted photocatalysis C–N coupling of benzylamine, *Nano Energy* 83 (2021) 105831.
- [58] Z.X. Wu, Y. Zhao, H.B. Wu, Y.X. Gao, Z. Chen, W. Jin, J.S. Wang, T.Y. Ma, L. Wang, Corrosion engineering on iron foam toward efficiently electrocatalytic overall water splitting powered by sustainable energy, *Adv. Funct. Mater.* 31 (2021) 2010437.
- [59] Y. Liu, P. Xu, Z. Ye, T. Cen, X. Peng, D. Yuan, H. Wu, P doped CoMoO₄/RGO as an efficient hybrid catalyst for hydrogen evolution, *Int. J. Hydrog. Energy* 45 (2020) 15157–15165.
- [60] X.B. Zhou, X.B. Liao, X.L. Pan, M.Y. Yan, L. He, P.J. Wu, Y. Zhao, W. Luo, L.Q. Mai, Unveiling the role of surface P–O group in P-doped Co₃O₄ for electrocatalytic oxygen evolution by On-chip micro-device, *Nano Energy* 83 (2021) 105748.
- [61] L.B. Wu, L. Yu, F.H. Zhang, B. McElhenny, D. Luo, A. Karim, S. Chen, Z.F. Ren, Heterogeneous bimetallic phosphide Ni₂P–Fe₂P as an efficient bifunctional catalyst for water/seawater splitting, *Adv. Funct. Mater.* 31 (2021) 2006484.
- [62] Y.-Z. Xu, C.-Z. Yuan, X.-P. Chen, A facile strategy for the synthesis of NiSe@CoOOH core-shell nanowires on nickel foam with high surface area as efficient electrocatalyst for oxygen evolution reaction, *Appl. Surf. Sci.* 426 (2017) 688–693.
- [63] J.A. Koza, C.M. Hull, Y.C. Liu, J.A. Switzer, Deposition of beta-Co(OH)₂ films by electrochemical reduction of tris(ethylenediamine)cobalt(III) in alkaline solution, *Chem. Mater.* 25 (2013) 1922–1926.
- [64] Y. Zeng, M. Zhao, Z. Huang, W. Zhu, J. Zheng, Q. Jiang, Z. Wang, H. Liang, Surface reconstruction of water splitting electrocatalysts, *Adv. Energy Mater.* 12 (2022) 2201713.
- [65] X. Liu, J.S. Meng, K. Ni, R.T. Guo, F.J. Xia, J.J. Xie, X. Li, B. Wen, P.J. Wu, M. Li, J. S. Wu, X.J. Wu, L.Q. Mai, D.Y. Zhao, Complete reconstruction of hydrate pre-catalysts for ultrastable water electrolysis in industrial-concentration alkali media, *Cell Rep. Phys. Sci.* 1 (2020) 100241.
- [66] Y. Wang, Y.L. Zhu, S.L. Zhao, S.X. She, F.F. Zhang, Y. Chen, T. Williams, T. Gengenbach, L.H. Zu, H.Y. Mao, W. Zhou, Z.P. Shao, H.T. Wang, J. Tang, D. Y. Zhao, C. Selomulya, Anion etching for accessing rapid and deep self-reconstruction of precatalysts for water oxidation, *Matter* 3 (2020) 2124–2137.
- [67] Z. Zhang, C. Feng, D. Wang, S. Zhou, R. Wang, S. Hu, H. Li, M. Zuo, Y. Kong, J. Bao, J. Zeng, Selectively anchoring single atoms on specific sites of supports for improved oxygen evolution, *Nat. Commun.* 13 (2022) 2473.
- [68] L. Nie, D.H. Mei, H.F. Xiong, B. Peng, Z.B. Ren, X.I.P. Hernandez, A. DeLariva, M. Wang, M.H. Engelhard, L. Kovarik, A.K. Datye, Y. Wang, Activation of surface lattice oxygen in single-atom Pt/CeO₂ for low-temperature CO oxidation, *Science* 358 (2017) 1419–1423.
- [69] A. Beniya, S. Higashi, Towards dense single-atom catalysts for future automotive applications, *Nat. Catal.* 2 (2019) 590–602.
- [70] Y. Zhang, J. Fu, H. Zhao, R. Jiang, F. Tian, R. Zhang, Tremella-like Ni₃S₂/MnS with ultrathin nanosheets and abundant oxygen vacancies directly used for high speed overall water splitting, *Appl. Catal. B: Environ.* 257 (2019) 117899.
- [71] B.H.R. Suryanto, Y. Wang, R.K. Hocking, W. Adamson, C. Zhao, Overall electrochemical splitting of water at the heterogeneous interface of nickel and iron oxide, *Nat. Commun.* 10 (2019) 5599.
- [72] G. Zhang, Y.-S. Feng, W.-T. Lu, D. He, C.-Y. Wang, Y.-K. Li, X.-Y. Wang, F.-F. Cao, Enhanced catalysis of electrochemical overall water splitting in alkaline media by Fe doping in Ni₃S₂ nanosheet arrays, *ACS Catal.* 8 (2018) 5431–5441.
- [73] J. Zhang, T. Wang, D. Pohl, B. Rellinghaus, R.H. Dong, S.H. Liu, X.D. Zhuang, X. L. Feng, Interface engineering of MoS₂/Ni₃S₂ heterostructures for highly enhanced electrochemical overall-water-splitting activity, *Angew. Chem. Int. Ed.* 55 (2016) 6702–6707.
- [74] Q. Chen, R. Ding, H. Liu, L. Zhou, Y. Wang, Y. Zhang, G. Fan, Flexible active-site engineering of monometallic Co-layered double hydroxides for achieving high-performance bifunctional electrocatalyst toward oxygen evolution and H₂O₂ reduction, *ACS Appl. Mater. Interfaces* 12 (2020) 12919–12929.